2024 IEEE/RSJ International Conference on Intelligent Robots and Systems (IROS)
October 14-18, 2024. Abu Dhabi, UAE

Advanced Handheld Micro-Surgical System using an Hall Sensor and a Magnet Trocar for Retinal Microsurgery

Myung Ho Lee[1], Jintaek Im[1], and Cheol Song[1†]

***Abstract*— Diseases affecting the retina, such as retinal detachment, diabetic retinopathy, and macular degeneration, are significant contributors to blindness globally, with a substantial risk of vision loss among those afflicted. Surgical treatment of these conditions is complex due to the delicate nature of retinal tissue and the challenges posed by involuntary hand movements. While existing methods aim to compensate for hand tremors using sensor-based systems, they are hindered by limitations in accurately tracking retinal surface movement during surgery, particularly in response to patient movements under anesthesia. To address these issues, this study proposes a novel handheld micro-surgical tool equipped with a 1-degree of freedom (DOF) mechanism and a 3-axis Hall sensor to mitigate physiological hand tremors effectively. By utilizing magnetic flux density measurements, the tool can pinpoint the position of a magnet embedded within the surgical instrument, enabling precise tremor compensation without reliance on a global coordinate system. The design incorporates a piezoelectric (PZT) linear actuator and a Hall sensor for compactness and sensitivity. Optimization of the magnet's dimensions through simulation ensures optimal sensor performance. Experimental validation using artificial and ex-vivo porcine eye models demonstrates the tool's effectiveness in reducing hand tremors, suggesting potential enhancements in the safety and accuracy of retinal surgeries. For the desired positions from 4000 µm to 1000 µm, the RMS error of the synthetic eye model and porcine eye decreased from 71.10 µm to 33.27 µm and 71.36 µm to 33.39 µm, respectively.**

I. Introduction

Retinal diseases, such as retinal detachment, diabetic retinopathy, and macular degeneration, are leading causes of blindness, with a 12% probability of vision loss among affected patients [1]. In a six-year statistical study of Americans [2], common types of retinal diseases exhibited approximately 160,000 new cases. Retinal surgery has been challenging to treat because micro nerves and blood vessels are intertwined [3]. For this reason, the reoperation rate for retinal surgery was almost 80 % [4], so surgeons should have excellent surgical skills and experience.

There are various difficulties in retinal surgery. First, the retina comprises many layers; each layer is very thin, 30 µm to 69 µm [5], [6]. The physiological hand tremor is about a magnitude of 108 µm and a frequency of 6 Hz [7], enough to damage the retina. Surgeons must have delicate hand skills for safe and precise retinal-related eye surgery. Also, getting sufficient vision inside the eye is difficult due to the narrow space and darkness during surgery. In addition, it is difficult to know the distance between the end of the surgical tool and the retina, which can damage the retina.

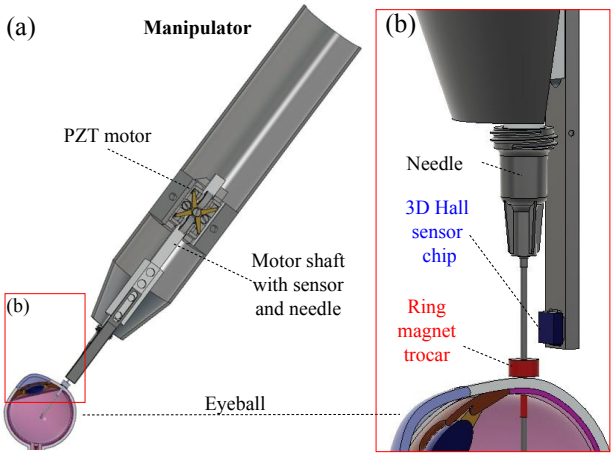

Fig. 1. (a) Configuration of the proposed manipulator. (b) 3-axis Hall sensor system with ring permanent magnet trocar

For these limitations, many studies have been conducted on surgical tools and hand tremor removal. One is to remove hand tremors in needle positions to measure and compensate for the tremors in surgical instruments, including physiological hand tremors from the global coordinate. For example, an inertial measurement unit (IMU) [8] with an accelerometer, a gyroscope, and a geomagnetic sensor, a MICRON [9] that tracks LEDs attached to surgical instruments with a 3D camera, and an Electromagnetic (EM) [10] are used to compensate for hand tremors and the positions of the ends of surgical instruments. However, these methods do not know the location of the retinal surface during surgery because hand tremors are compensated in the global coordinate system. In the case of surgery performed by a patient under anesthesia, a body movement of the patient's breathing or an unspecified movement of the involuntary muscle occurs, which causes a continuous change in the target retina position [11]. Patients who are not anesthetized have more severe movement. The above methods make it challenging to respond to these movements.

The other is a handheld manipulator to overcome these surgical difficulties by introducing optical coherence tomog-

† Corresponding author
[1]Department of Robotics and Mechatronics Engineering, DGIST, Daegu 42988, South Korea (Lmho777, wlsehd23,csong)@dgist.ac.kr

*This work was supported by the Technology Innovation Program(20023168, Development of clinician collaborative robot platform technology for 3 types of pain interventional procedures based on crossdrug handler and instrument modules) funded by the Ministry of Trade of Trade, Industry & Energy(MOTIE, Korea) and the DGIST R&D Program of the Ministry of Science, ICT and Technology of Korea (24-N-HRHR-02).We are thankful for the simple discussion with Mr.John Prada.

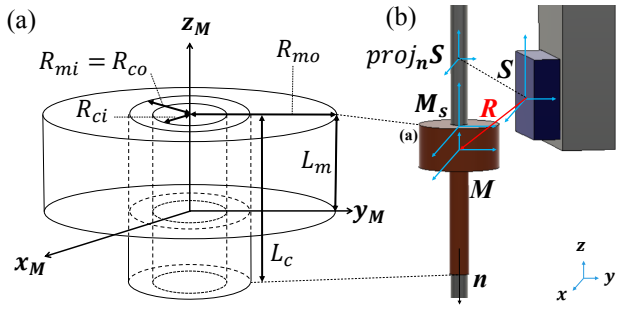

Fig. 2. (a) The proposed trocar consists of a ring permanent magnet and metal cannulas. Dimensions of the ring permanent magnet are an inner radius: R_{mi}, an outer radius: R_{mo}, and a height: L_m. Dimensions of the metal cannulas are an inner radius: R_{ci}, an outer radius: R_{co}, and a height: L_c. (b) Illustration of the measurement system consisting of a ring permanent magnet and a 3-axis Hall sensor.

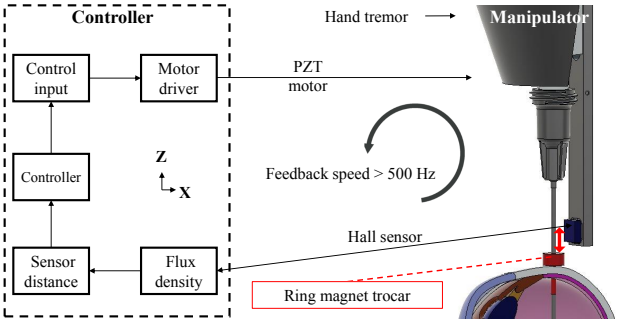

Fig. 3. Schematic of handheld 1-DOF surgical tool based on 3-axis Hall sensor-magnet trocar localization and feedback control scheme at an update speed of 500 Hz.

raphy [12–14]. The Smart Micromanulation Aided Robotic-Surgery Tool (SMART) system is a portable surgical tool [15–19]. The system was developed to prevent the retina from being damaged by hand tremors using a common path swept-source optical coherence tomography (CP-SSOCT) distance sensor [20], [21]. The CP-SSOCT distance sensor used in this SMART system has excellent resolution and a high-speed sampling rate, so it can accurately measure hand tremors [22], [23]. However, extending the system is difficult due to the short detectable distance and the need for reflective surfaces. In addition, since the optical fiber is fixed to the injection needle, it is difficult to replace it in actual surgery. Also, if the fiber is broken or disassembled due to the needle movement during the surgery, tiny fiber pieces in the eye are likely to cause tissue damage. Lastly, there is an inherent risk of directly irradiating the retina with optical laser light.

With compensating for hand tremors while overcoming the limitations and risks arising from prior research, this study presents a 1-degree of freedom (DOF) handheld micro-surgical tool based on one actuator and a 3-axis Hall sensor to remove the physiological hand tremors of surgeons. The Hall sensor, which can find the location of the magnet, has the characteristic of overcoming the short range of the OCT distance sensor used in previous studies. One piezoelectric (PZT) linear actuator and one Hall sensor were used for miniaturization. To measure hand tremors with magnetic flux density, a trocar as a channel of the eye surgical tool was fabricated and modeled from a ring-type neodymium permanent magnet. The dimension of the magnet was optimized by considering the sensitivity and sensing range of the sensor using simulation software. The distance between the trocar on the sclera and the sensor was measured through magnet positioning instead of the global coordinate system. Therefore, it can respond to the unspecified movements of the patient. To validate the efficacy of the surgical tool, we assessed the sensor hysteresis error and performed sensor calibration. Also, experiments are conducted to remove actual hand tremors using an artificial eye model and an *ex-vivo* porcine eye.

II. System Design and Method

A. Micro-surgical Tool System

We designed the prototype of a handheld surgical manipulator featuring one PZT motor and a tool housing, including a body and cover, as shown in Fig. 1(a). The PZT motor (LEGS-L01S-11, PiezoMotor) consists of a motor and a shaft with a Hall sensor (TMAG5170, Texas Instruments) bar and a detachable 25G needle. The sensor chip is on the end of the bar, and its length is adjustable. In an actual surgical environment, a trocar as an insertion channel tool is used when a needle is inserted into the eyeball. In this study, a specially designed trocar combined with a magnet is fabricated and used. A Hall sensor attached to the end of the bar coupled to the shaft of the PZT motor measures hand tremors by measuring the distance from the magnet fixed to the eyeball.

B. Ring Magnet Trocar Design

The trocar cannula system is used in ophthalmic surgery to access the inside of the eye by providing an entrance for other surgical instruments, such as needles or forceps [24]. The trocar is placed in the sclera, the outer protective layer of the eye, through a small incision made with an insertion knife. The trocar system consists of a metal cannula as a channel and a valve at the top. Generally, the size of the cannula is 23G (0.64 mm), 25G (0.51 mm), and 27G (0.40 mm) [24], and the inner and outer diameters of 23G and 22G were used in this study. The length L_c of the cannula is about 4 mm long enough to reach the inner cavity of the eye and not long enough to damage the inner structure [25]. The difference from the existing system is that a chrome-coated neodymium magnet was used in the valve instead of a plastic object. As shown in Fig. 2(a), the ring magnets were fabricated with an inner diameter of $2 * R_{mi}$ of 0.7 mm, an outer diameter of $2 * R_{mo}$ of 2 mm, and a height of L_m of 1 mm to couple to the metal cannula.

C. Ring Magnet Localization

It is necessary to know the location of the manufactured magnetic trocar cannula as a Hall sensor on the surgical instrument. Hence, assuming a distance z between the ring magnet and the sensor, we defined the scalar

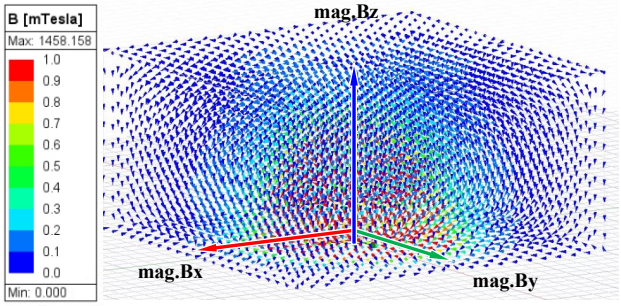

Fig. 4. Magnetic field vector of ring permanent magnet. The magnetic flux density of each axis is measured based on the three color lines using the ANSYS Electronics Desktop (AEDT) software.

potential$\phi_{axiz}(z)$ and magnetic flux density in the Z-axis $B(z)$ as follows [26]:

$$\phi_{axiz}(z) = \frac{M}{2}[(\sqrt{(z-L)^2+R_{mo}^2} - \sqrt{z^2+R_{mo}^2}) - (\sqrt{(z-L)^2+R_{mi}^2} - \sqrt{z^2+R_{mi}^2})] \quad (1)$$

$$B(z) = \frac{M}{2}[(\frac{z}{\sqrt{z^2+R_{mo}^2}} - \frac{z-L}{\sqrt{(z-L)^2+R_{mo}^2}}) - (\frac{z}{\sqrt{z^2+R_{mi}^2}} - \frac{z-L}{\sqrt{(z-L)^2+R_{mi}^2}})] \quad (2)$$

Since the 3-axis Hall sensor can measure the magnetic flux density in three dimensions, we denoted the magnetic flux density of magnets **B** as follows [27]:

$$\mathbf{B} = M_T(\frac{3(\mathbf{H_0}\cdot\mathbf{P})\mathbf{P}}{R^5} - \frac{\mathbf{H_0}}{R^3}) \quad (3)$$

where the vector **P** indicates the position of the magnet from the sensor and is expressed as (d_x, d_y, d_z). In addition, the vector $\mathbf{H_0}$ represents the polar direction of the magnet (m, n, p). Moreover, we calculated the magnetization constant related to the magnet M_T as follows:

$$M_T = \frac{\mu_0\mu_r L_0 M_0}{4}(R_{mo}^2 - R_{mi}^2) \quad (4)$$

where $\mu_0 = 4\pi * 10^{-7}[H/m]$ and μ_r represent the vacuum permeability and relative permeability, respectively. Furthermore, from Equation (3), we calculated the magnetic flux density of the three orthogonal components as follows [28]:

$$B_x = M_T\{\frac{3[m(x-d_x)+n(y-d_y)+p(z-d_z)](x-d_x)}{R^5} - \frac{m}{R^3}\} \quad (5)$$

$$B_y = M_T\{\frac{3[m(x-d_x)+n(y-d_y)+p(z-d_z)](y-d_y)}{R^5} - \frac{n}{R^3}\} \quad (6)$$

$$B_z = M_T\{\frac{3[m(x-d_x)+n(y-d_y)+p(z-d_z)](z-d_z)}{R^5} - \frac{p}{R^3}\} \quad (7)$$

Assuming that the x, y, and z components from the Equations (5)-(7) are all zero, we can simplified B_x, B_y and B_z as follows:

$$B_x = M_T\{\frac{3d_x(md_x+nd_y+pd_z]}{R^5} - \frac{m}{R^3}\} \quad (8)$$

$$B_y = M_T\{\frac{3d_y(md_x+nd_y+pd_z]}{R^5} - \frac{n}{R^3}\} \quad (9)$$

$$B_z = M_T\{\frac{3d_z(md_x+nd_y+pd_z]}{R^5} - \frac{p}{R^3}\} \quad (10)$$

The vector *R*, which is marked in red color, is the distance between the sensor and the ring magnet, as shown

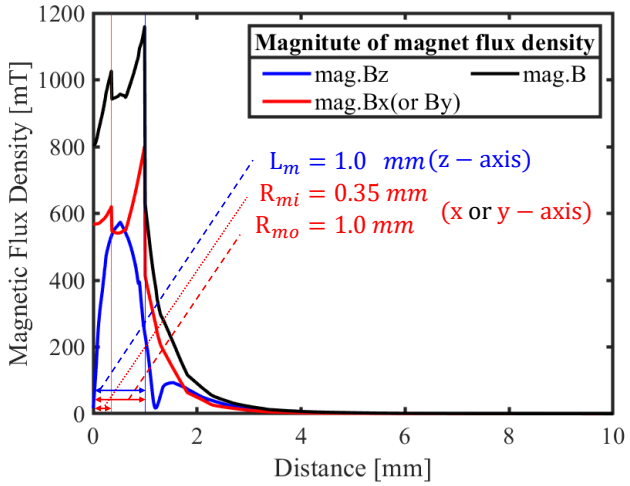

Fig. 5. Measured magnetic flux density for each axis from the ANSYS Electronics Desktop (AEDT) software. The height L_m, the inner radius R_{mi}, and the outer radius R_{mo} of the magnet were indicated.

in Fig. 2(b). The distance can be defined and calculated as follows:

$$R = \{d_x, d_y, d_z\}^T \quad (11)$$

$$\|R\| = \sqrt{d_x^2 + d_y^2 + d_z^2} \quad (12)$$

Since there are three variables (d_x, d_y, d_z) and three Equations (8)-(10), (d_x, d_y, d_z) can be calculated. Then, $\mathbf{B} = (Bx, By, Bz)$ is a vector measured by a three-axis Hall sensor. The distance vector between the sensor $\boldsymbol{S}$ and the projection vector $\boldsymbol{proj_n S}$ of sensor on the needle axis $\boldsymbol{n}$ is a fixed distance vector that includes constant values. It can be expressed as follows:

$$\overline{\boldsymbol{S}\,\boldsymbol{proj_n}\,\boldsymbol{S}} = \{d_{xc}, d_{yc}, d_{zc}\}^T \quad (13)$$

Finally, the distance between the surgical tool and the center of the ring magnet trocar was calculated. Since the equations for calculating the magnetic flux density are the distance from the magnet's center, the distance to the magnet's surface must be calculated. As shown in Fig. 2(b), $\boldsymbol{M_s}$ is a coordinate located on the surface of a magnet. The distance to the surface can be calculated by subtracting half the length of the ring magnet from the sensor-magnet center length. This is the distance between the actual tool and the surface of the magnet, which is used as a control variable:

$$R_{eff} = \overline{\boldsymbol{M_s}\,\boldsymbol{proj_n}\,\boldsymbol{S}} = \sqrt{R^2 - \overline{\boldsymbol{S}\,\boldsymbol{proj_n}\,\boldsymbol{S}}^2} - \overline{\boldsymbol{M_s M}} = \sqrt{d_x^2 - d_{xc}^2 + d_y^2 - d_{yc}^2 + d_z^2 - d_{zc}^2} - \frac{L_m}{2} \quad (14)$$

D. Control: Hand tremor removing

The system consists of the manipulator and controller, as shown in Fig. 3 The controller includes a motor driver and an Arduino for measuring sensor values. The Visual Studio Microsoft Foundation Class (MFC) built the feedback control system in the C++ language. The serial peripheral interface (SPI) communication connects the sensor to the

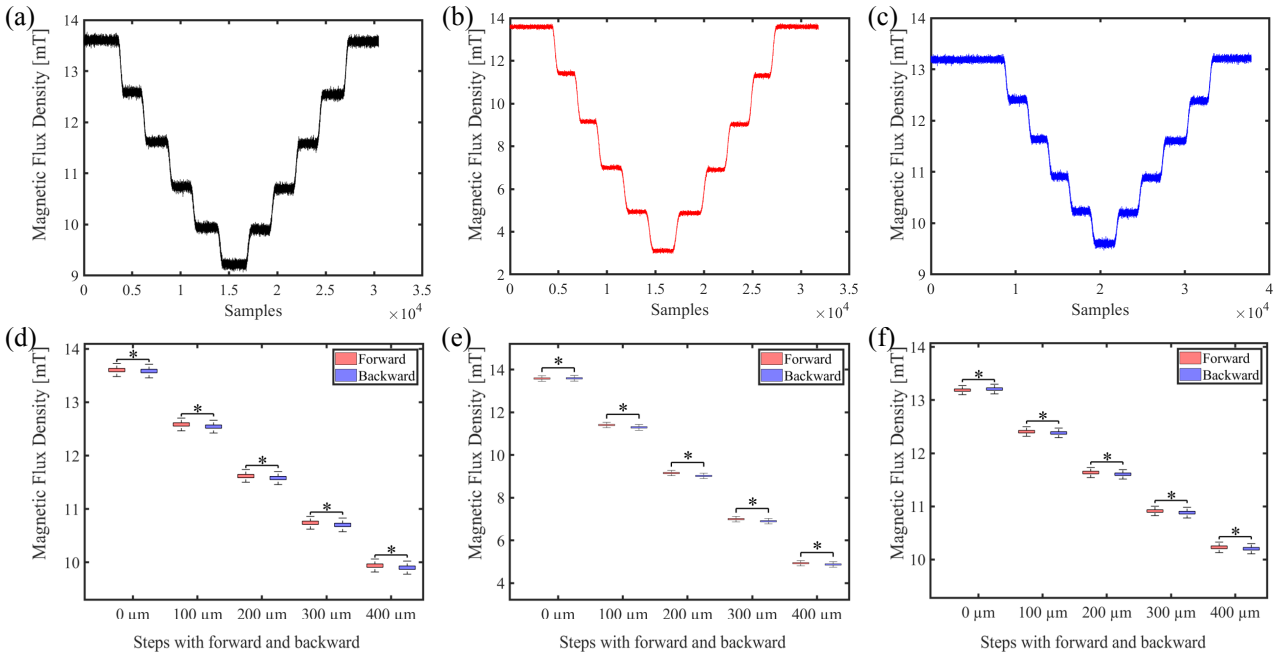

Fig. 6. Measured Hysteresis result of each axis. Magnetic flux density by five steps forward and backward input in (a) the vector **B**, (b) the X or Y-axis, and (c) the Z-axis. The box plots of the magnetic flux density at each step along (d) the vector **B**, (e) the X or Y-axis, and (f) the Z-axis. ($*$ p<0.001)

Arduino. As a manipulation for surgery, hand tremors affect the manipulator. The 3-axis magnetic flux density between the 3-axis Hall sensor and the ring magnet trocar is measured. Each measured magnetic flux density was calculated as equations of the distance-sensor values. After calculating the actual distance between the magnet surface and the Hall sensor obtained above, it was used for PID control. At this time, hand tremors were compensated by the PZT motor control. Since the performance of the 3-axis Hall sensor exceeds 500 Hz, a control loop can remove hand tremors. It was possible to measure and compensate for hand tremors sufficiently [18].

III. Magnetic Flux Density Simulation

A. Simulation Environments

We acquired the simulation results using the ANSYS Electronics Desktop (AEDT) software, as shown in Fig. 4 and Fig. 5. A ring neodymium permanent magnet was designed to be the same size as the actual dimension. The medium of the magnet was set to NdFe35. The boundary range around the magnet was set to $20 \times 20 \times 10\,\mathrm{mm}$, and the medium was set to air. Fig. 4 shows the magnetic field vector in three dimensions. The measurement range was set by drawing three color lines to measure the magnetic flux density for each target displacement of each axis. Since the designed magnet has rotational symmetry about the Z-axis, the magnitude of $\mathbf{B_x}$ and $\mathbf{B_y}$ are the same. Fig. 5 shows the magnitude of the vector **B**, $\mathbf{B_x}$, $\mathbf{B_y}$, and $\mathbf{B_z}$, where $\mathbf{B_x} = \mathbf{B_y}$. It represents the changing magnetic flux density at the magnet surface in each axis. The colored longitudinal axes represent the height L_m, the inner radius R_{mi}, and the outer radius R_{mo} of the magnet.

B. Simulation Results

Fig. 5 shows the magnetic flux density around the magnet by distance in each axis. The blue line represents the change in the magnetic flux density within $10\,\mathrm{mm}$ in the X-axis direction. The red line represents the change in the magnetic flux density within $10\,\mathrm{mm}$ in the x or Y-axis direction. The black line represents the change in the magnetic flux density within $10\,\mathrm{mm}$ of the vector **B**. Since the designed ring-shaped magnet is rotationally symmetrical around the Z-axis, the values of the magnetic flux density in the x and y axes are the same. Therefore, the change in the magnetic flux density within $10\,\mathrm{mm}$ in the X-axis direction of the red arrow and the change in the magnetic flux density within $10\,\mathrm{mm}$ in the Y-axis direction of the green arrow is the same, as shown in Fig. 4. The magnetic flux density values of the X-axis and Y-axis are displayed in red, as shown in Fig. 5. The vertical axes indicate the surface position of the magnet, the blue dashed line indicates the height of the magnet at $1.0\,\mathrm{mm}$, and the red dashed lines indicate the inner radius of the hollow ring

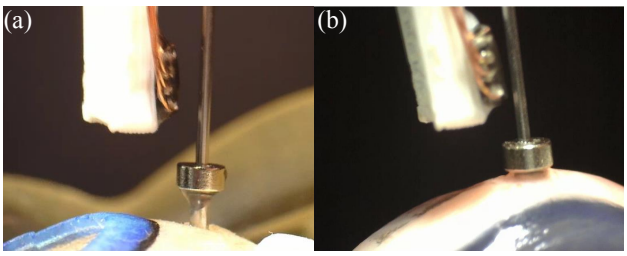

Fig. 7. Experimental samples. (a) An artificial eye model and (b) an *ex-vivo* porcine eye were used to evaluate the control performance.

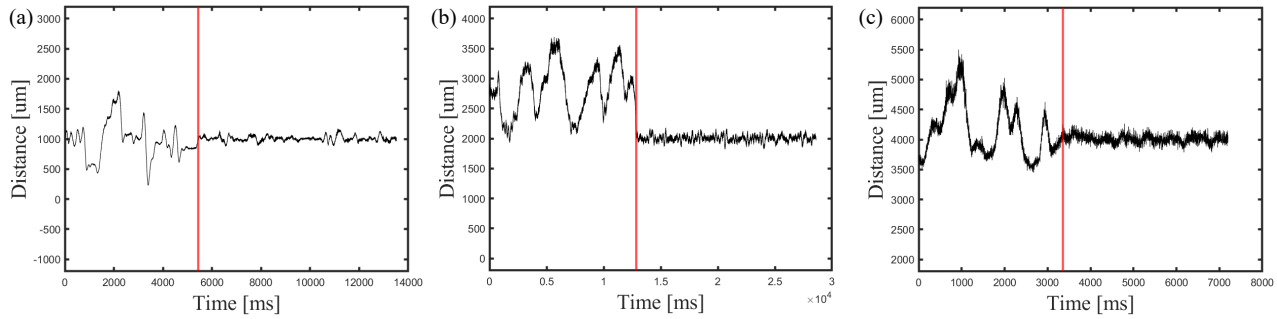

Fig. 8. The results of hand tremor compensation using an artificial eye model. Before and after, according to the red line. (a) Converted distance by the desired position as 1000 µm. (b) Converted distance by the desired position as 2000 µm. (c) Converted distance by the desired position as 4000 µm.

magnet of 0.35 mm and the outer radius of 1.0 mm. The region of interest is the magnetic flux density on the surface. There are the values after 1.0 mm in the Z-axis of the blue, the X-axis of the red, and the **B** of the black.

IV. Sensor Calibration

A. Hysteresis Error Measurement

To evaluate the sensor performance, the hysteresis errors of the sensor were measured by moving forward and backward five steps at 0.1 mm in the vector **B**, the X or Y-axis, and the Z-axis, respectively. The value was measured by changing the distance of the sensor and magnet to a precise motorized translation stage (MT1-Z8, Thorlab) driven by a motor controller (KDC101, Thorlab). The sensor value of a 3-axis Hall sensor is measured in [mT] units with magnetic flux density, which changes depending on the distance to the magnet. In other words, in this experiment, we can experimentally define the relationship between the magnetic flux density and distance between the sensor and the magnet trocar.

B. Calibration: Magnetic Flux Density to Distance

The hysteresis values of the sensor were measured by moving forward and backward five steps at 0.1 mm, as shown in Fig. 6(a)-(c). The plots indicate the magnetic flux density of the vector **B**, $\mathbf{B_x}$, and $\mathbf{B_z}$. In addition, we made the box plots of the magnetic flux density measured in each step along the vector **B**, the X or Y-axis, and the Z-axis, as shown in Fig. 6(d)-(f). Moreover, the red and blue boxes represent the magnetic flux density in the forward and backward directions, respectively. The black graph of vectors **B** obtained by the simulation in Fig. 5 and the actual measurement in Fig. 6(a) is the same data value, but there is a gap between the simulation and physical magnetic fields. This is why sensor calibration, as well as sensor simulation, should be based on real measurements. In addition, a t-test was conducted between the forward and backward results from magnetic flux density at each step with a significance level of $p<0.01$. Therefore, for all cases, we obtained $p<0.001$. Also, we calculated the RMS error between the forward and backward data from the sensor. We found maximum RMS errors of 0.25 mT, 0.03 mT, and 0.24 mT of the vectors **B**, $\mathbf{B_x}$, and $\mathbf{B_z}$, respectively. Furthermore, we implemented a two-term exponential model to calibrate distance-sensor values. The relationship between the distance and the magnitude of the magnetic flux density was defined as the parametric equation. For the tremor compensation task, the magnitude of the magnetic flux density was converted to a distance value and used as a control parameter.

V. Experiments and Results

A. Hand Tremor Removal Experimental Setup

An experiment to remove hand tremors was conducted using a calibrated 3-axis Hall sensor and a ring magnet trocar with the handheld surgical tool. An artificial eye model (fundus-globe model, Bioniko) was used to evaluate the control performance, and an experiment was performed on an *ex-vivo* porcine eye. The position of the ring magnet surface and the sensor were set to 1000 µm, 2000 µm, and 4000 µm, respectively. It was divided before and after the control function to remove hand tremors. After measuring the value of the three-axis Hall sensor, the magnitude of hand tremors was compared before and after the tool-aided motion. The person who measured hand tremors was conducted with an untrained public member.

B. Results of Hand Tremor Removal Experiments

We used an artificial eye model to evaluate the control performance, as shown in Fig. 8. We mapped the magnetic flux density into distance metric, targeting desired positions of 1000 µm, 2000 µm, and 4000 µm, as shown in Fig. 8(a)-(c). Also, we used an *ex-vivo* porcine eyeball to evaluate the control performance, as shown in Fig. 9. Similar to the artificial eye model evaluation, we converted the flux density values into distance information, aiming to fix positions of 1000 µm, 2000 µm, and 4000 µm, as shown in Fig. 9(a)-(c). In addition, we compared the sensor information, including the position and amplitude of hand tremors before and after activating the system. A red horizontal line represents the moment when the system was triggered, as shown in Fig. 8 and Fig. 9. Moreover, we calculated the RMS error values of the evaluations from the artificial eye model and porcine eye, as shown in Table I. In general, the RMS error decreases as the desired position gets lower. For the desired positions from 4000 µm to 1000 µm, the RMS error of the artificial

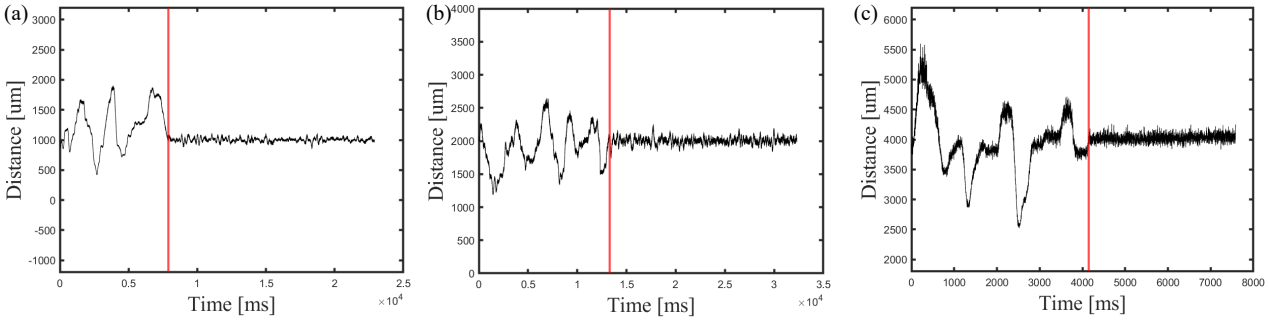

Fig. 9. The results of hand tremor compensation using an *ex-vivo* porcine eyeball. Before and after, according to the red line. (a) Converted distance by the desired position as 1000 µm. (b) Converted distance by the desired position as 2000 µm. (c) Converted distance by the desired position as 4000 µm.

eye model and porcine eye decreased from 71.10 µm to 33.27 µm and 71.38 µm to 33.39 µm, respectively.

TABLE I
RMS ERROR OF COMPENSATING HAND TREMOR

Desired position	1000 µm	2000 µm	4000 µm
An eye model	33.27 µm	51.39 µm	71.10 µm
A porcine eye	33.39 µm	52.81 µm	71.38 µm

VI. DISCUSSION AND CONCLUSION

We implemented a handheld micro-surgical tool for micro-surgery based on the 3-axis Hall sensor with magnet localization. The micro-surgical tool comprises a Piezoelectric linear motor and a 3-axis Hall sensor. A trocar used as an entrance to the surgical tool was manufactured with a ring-type permanent magnet to measure the distance between the Hall sensor and the eyeball. The magnetic flux density measured by the 3-axis Hall sensor was used to determine the magnet's position. The RMS error at the desired position of 1000 µm using synthetic and porcine eyes were 33.27 µm and 33.39 µm, respectively. The axial RMS error of the SMART system, a previous study, is 9.23 µm, smaller than this study's. However, the laser equipment used in the SMART system is relatively expensive and dangerous because a fragile optical fiber is attached to the needle and inserted into the eye. Instead of using the OCT sensor, we successfully implement a micro-surgical tool with a relatively inexpensive 3-axis Hall sensor and a ring magnet trocar. Furthermore, we will implement the 3-axis Hall sensor in a multi-DOF parallel platform surgical tool in future works. In addition, we will apply multiple 3-axis Hall sensors to measure the position of the magnet more accurately. Also, we plan to use multi-axis sensing to measure the position and orientation of the ring magnet trocar.

REFERENCES

[1] C. M. Ramsden, M. B. Powner, A.-J. F. Carr, M. J. Smart, L. da Cruz, and P. J. Coffey, "Stem cells in retinal regeneration: past, present and future," *Development*, vol. 140, no. 12, pp. 2576–2585, 2013.

[2] T. R. Rosenblatt, D. Vail, N. Saroj, N. Boucher, D. M. Moshfeghi, and A. A. Moshfeghi, "Increasing incidence and prevalence of common retinal diseases in retina practices across the united states," *Ophthalmic Surgery, Lasers and Imaging Retina*, vol. 52, no. 1, pp. 29–36, 2021.

[3] J. S. Kim, J. Chhablani, C. K. Chan, L. Cheng, I. Kozak, K. Hartmann, and W. R. Freeman, "Retinal adherence and fibrillary surface changes correlate with surgical difficulty of epiretinal membrane removal," *American journal of ophthalmology*, vol. 153, no. 4, pp. 692–697, 2012.

[4] P. Sullivan, A. Luff, and G. Aylward, "Results of primary retinal reattachment surgery: a prospective audit," *Eye*, vol. 11, no. 6, pp. 869–871, 1997.

[5] A. M. Bagci, M. Shahidi, R. Ansari, M. Blair, N. P. Blair, and R. Zelkha, "Thickness profiles of retinal layers by optical coherence tomography image segmentation," *American journal of ophthalmology*, vol. 146, no. 5, pp. 679–687, 2008.

[6] S. Grover, R. K. Murthy, V. S. Brar, and K. V. Chalam, "Comparison of retinal thickness in normal eyes using stratus and spectralis optical coherence tomography," *Investigative ophthalmology & visual science*, vol. 51, no. 5, pp. 2644–2647, 2010.

[7] R. Elble and W. Koller, "Unusual forms of tremor," *Tremor, The Johns Hopkins University Press, Baltimore*, pp. 154–157, 1990.

[8] W. T. Ang, P. Pradeep, and C. Riviere, "Active tremor compensation in microsurgery," in *The 26th Annual International Conference of the IEEE Engineering in Medicine and Biology Society*, vol. 1. IEEE, 2004, pp. 2738–2741.

[9] S. Yang, R. A. MacLachlan, and C. N. Riviere, "Manipulator design and operation of a six-degree-of-freedom handheld tremor-canceling microsurgical instrument," *IEEE/ASME transactions on mechatronics*, vol. 20, no. 2, pp. 761–772, 2014.

[10] E. Kim, I. Choi, and S. Yang, "Design and control of fully handheld microsurgical robot for active tremor cancellation," in *2021 IEEE International Conference on Robotics and Automation (ICRA)*. IEEE, 2021, pp. 12 289–12 295.

[11] W. M. Gild, K. L. Posner, R. A. Caplan, and F. W. Cheney, "Eye injuries associated with anesthesia. a closed claims analysis." *Anesthesiology*, vol. 76, no. 2, pp. 204–208, 1992.

[12] D. Huang, E. A. Swanson, C. P. Lin, J. S. Schuman, W. G. Stinson, W. Chang, M. R. Hee, T. Flotte, K. Gregory, C. A. Puliafito, and J. G. Fujimoto, "Optical coherence tomography," *Science*, vol. 254, no. 5035, pp. 1178–1181, 1991.

[13] C. Song, M. Ahn, and D. Gweon, "Polarization-sensitive spectral-domain optical coherence tomography using a multi-line single camera spectrometer," *Opt. Express*, vol. 18, no. 23, pp. 23 805–23 817, Nov 2010.

[14] D. Wang, J. Zhang, L. Liu, Z. Yan, P. Wang, Y. Ding, and H. Xie, "Application of oct for osteonecrosis using an endoscopic probe based on an electrothermal mems scanning mirror," *International Journal of Optomechatronics*, vol. 15, no. 1, pp. 87–96, 2021.

[15] C. Song, P. L. Gehlbach, and J. U. Kang, "Active tremor cancellation by a "smart" handheld vitreoretinal microsurgical tool using swept source optical coherence tomography," *Optics express*, vol. 20, no. 21, pp. 23 414–23 421, 2012.

[16] C. Song, P. L. Gehlbach, and J. Kang, "Swept source optical coherence tomography based smart handheld vitreoretinal microsurgical tool for tremor suppression," in *2012 Annual International Conference of the IEEE Engineering in Medicine and Biology Society*, 2012, pp. 1405–1408.

[17] C. Song, P. L. Gehlbach, and J. U. Kang, "Ball lens fiber optic sensor based smart handheld microsurgical instrument," in *Optical Fibers*

and Sensors for Medical Diagnostics and Treatment Applications XIII, I. Gannot, Ed., vol. 8576, International Society for Optics and Photonics. SPIE, 2013, p. 85760I.

[18] C. Song, D. Y. Park, P. L. Gehlbach, S. J. Park, and J. U. Kang, "Fiber-optic oct sensor guided "smart" micro-forceps for microsurgery," *Biomed. Opt. Express*, vol. 4, no. 7, pp. 1045–1050, Jul 2013.

[19] H. C. Park, C. B. Yeo, P. L. Gehlbach, and C. Song, "Development of the dual smart micro-surgical system using common-path swept source optical coherence tomography," in *2015 37th Annual International Conference of the IEEE Engineering in Medicine and Biology Society (EMBC)*, 2015, pp. 5–8.

[20] D. Koo, H.-C. Park, P. L. Gehlbach, and C. Song, "Development and preliminary results of bimanual smart micro-surgical system using a ball-lens coupled oct distance sensor," *Biomedical optics express*, vol. 7, no. 11, pp. 4816–4826, 2016.

[21] C. Yeo, H.-C. Park, S. Jang, P. L. Gehlbach, and C. Song, "Dual optical coherence tomography sensor guided, two-motor, horizontal smart micro-scissors," *Optics letters*, vol. 41, no. 20, pp. 4723–4726, 2016.

[22] J. Im and C. Song, "Oblique injection depth correction by a two parallel oct sensor guided handheld smart injector," *Biomed. Opt. Express*, vol. 12, no. 2, pp. 926–939, 2021.

[23] J. Im, S. Park, and C. Song, "Handheld motorized injection system with fiber-optic distance sensors and adaptive time-delay controller," *Int. J. Optomechatronics*, vol. 18, no. 1, p. 2299023, 2024.

[24] S. Mohamed, C. Claes, C. W. Tsang *et al.*, "Review of small gauge vitrectomy: progress and innovations," *Journal of ophthalmology*, vol. 2017, 2017.

[25] K. Lussenburg, M. Scali, A. Sakes, and P. Breedveld, "Additive manufacturing of a miniature functional trocar for eye surgery," *Frontiers in Medical Technology*, vol. 4, p. 842958, 2022.

[26] J. M. Camacho and V. Sosa, "Alternative method to calculate the magnetic field of permanent magnets with azimuthal symmetry," *Revista mexicana de física E*, vol. 59, no. 1, pp. 8–17, 2013.

[27] D. K. Cheng *et al.*, *Field and wave electromagnetics*. Pearson Education India, 1989.

[28] C. Hu, M. Q. Meng, and M. Mandal, "Efficient magnetic localization and orientation technique for capsule endoscopy," in *2005 IEEE/RSJ International Conference on Intelligent Robots and Systems*. IEEE, 2005, pp. 628–633.